Available online at www.sciencedirect.com
ScienceDirect
Ceramics International 35 (2009) 2951–2958
CERAMICS INTERNATIONAL
www.elsevier.com/locate/ceramint

Kirkendall porosity in barium titanate–strontium titanate diffusion couple

Cyuan-You Siao, Hwan-Wen Lee, Hong-Yang Lu *

Centre for NanoScience, Department of Materials Science, National Sun Yat-Sen University, Kaohsiung 80424, Taiwan

Received 9 March 2009; received in revised form 14 March 2009; accepted 2 April 2009
Available online 3 May 2009

Abstract

Inter-diffusion between perovskites $BaTiO_3$ and $SrTiO_3$ diffusion couple has been studied by determining the crystalline phases and analyzing the microchemistry and microstructure of undoped $BaTiO_3$–$SrTiO_3$ stacks sintered at 1250 °C in air. The Kirkendall effect manifested by: (1) an inter-diffusion zone containing $(Ba_{1-x}Sr_x)TiO_3$ and $(Sr_{1-x}Ba_x)TiO_3$ solid solutions, (2) the migration of the initial $BaTiO_3$–$SrTiO_3$ interface, and (3) the Kirkendall porosity was observed. The inter-diffused regions on both sides of the initial interface contain grains exhibiting the characteristic core–shell structure with distinctive solute contents between core and shell. TiO_2-rich polytitanates, notably $Ba_4Ti_{13}O_{30}$ and $Ba_6Ti_{17}O_{40}$ containing a minor amount of Sr from inter-diffusion, have been detected at the $BaTiO_3$ side near the initial $BaTiO_3$–$SrTiO_3$ interface. An analogy between the $BaTiO_3$–$SrTiO_3$ diffusion couple and Kirkendall's original α-brass-Cu couple is presented.

Keywords: A. Sintering; B. Electron microscopy; C. Microstructure-final; D. $BaTiO_3$ and titanates; E. Kirkendall effect

1. Introduction

The complete solid solution between perovskites $BaTiO_3$ and $SrTiO_3$ offers a wide range of applications for bulk as well as thin-film ceramics [1,2]. Tunable ferroelectrics of (Ba_xSr_y)-TiO_3 solid solutions has recently been investigated for their applications in microwave devices [1]. The dielectric properties characterized by a diffuse-phase transition are usually attributed to the microstructure consisting of core–shell grains [3,4]. The core and shell of distinctive chemical compositions comes from the inter-diffusion between two end-members during sintering.

The inter-diffusion of $CaTiO_3$–$SrTiO_3$ [5] and $BaTiO_3$–$SrTiO_3$ [6,7] couples has been reported. The Kirkendall effect was investigated [6] for hot-pressed and annealed $BaTiO_3$–$SrTiO_3$ samples, where Kirkendall porosity was observed, the inter-diffusion (or chemical diffusion) coefficient determined, and a theoretical model developed. In contrast to diffusion couples in metals, e.g. α-brass-Cu [8], Ni–Ti [9], the migration of all species, including both cations and oxygen, across the interface in the inter-diffusion of such complex oxides [6] is required for the effect to be realized. However, no observation of Kirkendall porosity by scanning electron microscopy (SEM) was reported by Butler et al. [5] when only inter-diffusion of Ca^{2+} and Sr^{2+} in $CaTiO_3$ and $SrTiO_3$ lattice, respectively, via a vacancy mechanism was found; the former cation was the faster diffusing species. Although Kirkendall-like porosity was again not detected experimentally in another study [7], it was thought to have retarded densification in a sintered $BaTiO_3$–$SrTiO_3$ powder mixture. Nevertheless, such porosity was observed [6] in the $BaTiO_3$ side of sintered La_2O_3-doped $BaTiO_3$–$SrTiO_3$ couple, followed by hot-pressing and annealing at 1300 °C for 48 h in air. The size of Kirkendall pores estimated directly from optical micrographs [6] was ~15–20 μm. Such observation [6] is an evidence of the Kirkendall effect, suggesting diffusion via a vacancy mechanism [5,6,8,9] when all species, including Ti^{4+} [6,10–12], via V''''_{Ti} (representing Ti vacancy using the Kröger–Vink notation) have moved and lattice migration by molecular diffusion occurred [6]. However, other than the interfacial voids of rather large sizes, neither microchemical analysis and phase identification to ensure cation inter-diffusion, nor microstructure analysis to reveal Kirkendall porosity has been adequately conducted.

We have analyzed the interface microstructure, aiming to resolve whether and where Kirkendall porosity is produced in the $BaTiO_3$–$SrTiO_3$ diffusion couple, and determined the crystalline phase in order to study the Kirkendall effect in multi-component ceramics. Sintering of two-layer stacks at

* Corresponding author. Fax: +886 7 5256030.
E-mail address: hyl@mail.nsysu.edu.tw (H.-Y. Lu).

0272-8842/$36.00
doi:10.1016/j.ceramint.2009.04.009

1250 °C in air was chosen in order that any liquid phase formed at >1332 °C by the $BaTiO_3$–$Ba_6Ti_{17}O_{40}$ eutectic [13] is avoided. This also allows the system to be considered as a simple pseudo-binary [6] when both are cubic in symmetry during sintering.

2. Experimental procedures

High-purity $BaTiO_3$ powder containing slightly TiO_2-excess at Ba/Ti = 0.9963 (Ticon HPB®, lot No. EXP19234) was supplied by Ferro Electronic Material Systems (Penn Yan, NY, U.S.A.). Major impurities in the powder as specified by the manufacturer are SiO_2 (<64 ppm), K_2O (<116 ppm), Fe_2O_3 (<8 ppm), CaO (<31 ppm), MgO (<2 ppm), ZrO_2 (<770 ppm), Na_2O (<35 ppm), and SrO (<64 ppm). $SrTiO_3$ powder of Sr/Ti = 0.999 (HPST-1, Fuji Titanium, Osaka, Japan) is also high purity and contains trace impurities of Fe_2O_3 (<10 ppm), Na_2O (<10 ppm) and CaO (<10 ppm).

The starting powders were separately ball milled for 24 h in isopropyl alcohol using Y_2O_3-stabilized ZrO_2 in a polyethylene bottle. Dried powder was de-agglomerated using an agate mortar and pestle, and passed through a 125 μm sieve. To make a stack, $BaTiO_3$ powder was die-pressed initially at 5 MPa to discs of 10 mm in diameter and ~1 mm thickness using a WC-inserted steel die. With the $BaTiO_3$ layer remained in the steel die, $SrTiO_3$ powder was added and die-pressed again at 100 MPa to make composite discs consisting of a $SrTiO_3$ layer stacked on top of $BaTiO_3$. The stacks loaded with α-Al_2O_3 plate on top were sintered at 1250 °C in air for several firing schedules.

The sintered samples were then cut with a diamond-embedded copper saw blade, ground mechanically using SiC papers successively to #1000, polished to <1 μm surface roughness by diamond lapping (Struers, Copenhagen, Denmark), and further polished with a SiO_2 slurry (Syton™ DuPont NanoMaterials, Carlsbad, CA, U.S.A.) before chemical-etching at room temperature in a solution of 30% HCl with a few drops of HF.

Crystalline phases of polished discs were determined by XRD (Siemens D5000, Karshrule, Germany) using Cu Kα radiation operating at 40 kV/30 mA. Microstructure was analyzed by SEM using a JEOL™ (Tokyo, Japan) SEM6330 equipped with a field-emission gun operating at 10–20 kV and the energy-dispersive spectroscopy (EDS, Link™ Systems, Oxford Instruments, Oxford, England). A thin layer of carbon was deposited on polished samples to avoid image drift in the microscope. Thin foils were prepared by the conventional technique of cutting, polishing, before Ar-ion milling (Duo-Mill® or PIPS®, Gatan, Pleasanton, CA, U.S.A.) to electron transparency. They were analyzed by the transmission electron microscopy (TEM) using JEOL™ AEM3010 operating at 300 kV.

3. Results

Sintering at 1250 °C was found to be an optimal temperature for the stacks to remain bonded, when delamination from differential sintering [14] or thermal expansion mismatch [6] was successfully prevented. The bonded stacks were initially examined under a reflected light optical microscope (OM). Sintered samples contained four regions of different solute content with distinctive microstructure, as confirmed by SEM and EDS. The cross-section microstructure is represented by samples sintered at 1250 °C for 40 h, where the four regions are designated (i), (ii), (iii), and (iv), as shown in Fig. 1. The $BaTiO_3$ layer is slightly concave upwards, as indicated by the straight (dotted) line drawn along the $BaTiO_3$–$SrTiO_3$ interface. The thickness of each layer in the samples studied here varies, depending on the extent of inter-diffusion induced by the heat treatment. Nevertheless, the characteristic pattern of the cross-section microstructure remains.

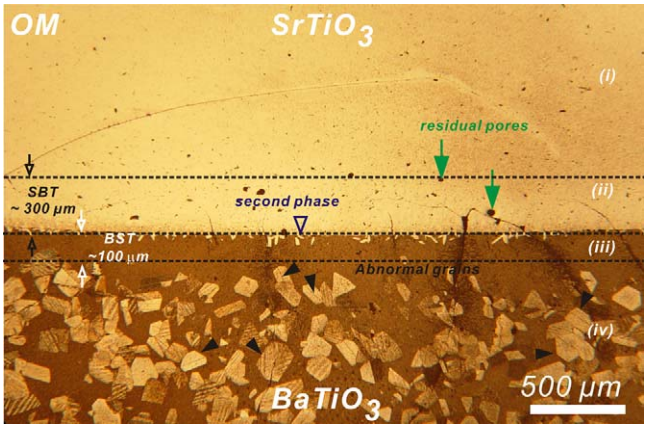

Fig. 1. Sintered microstructure is characterized by four distinctive regions designated (i), (ii), (iii) and (iv) (OM).

3.1. Crystalline phases

$BaTiO_3$ discs sintered alone at 1250 °C for 100 h reveals extra reflections representing $Ba_6Ti_{17}O_{40}$ (JCPDS 35-0817) and $Ba_6Ti_{17}O_{40-x}$ (JCPDS 43-0559). Such second phases often reported [3,15] in sintered $BaTiO_3$ ceramics are most likely resulted from $BaTiO_3$ reacting with the excess TiO_2 associated with the initial powder. No extra phases were detected in $SrTiO_3$ sintered under similar conditions by XRD.

The XRD patterns corresponding to regions (i)–(iv) (from samples sintered at 1250 °C/40 h) are shown in Fig. 2. They were obtained from the topmost surface (i.e. region (i)) before it was then ground off for phase determination using XRD for the next layer (i.e. regions (ii)), and successively for regions (iii) and (iv). Regions (i) and (iv) not affected by inter-diffusion have remained $SrTiO_3$ and $BaTiO_3$, whose reflection peaks are indexed according to JCPDS 35-0734 (cubic-$SrTiO_3$) and 05-0626 (tetragonal-$BaTiO_3$), respectively. The reflections of $SrTiO_3$ represented by {2 0 0} as framed in pattern (ii) show a distinctive left shoulder (indicated by an arrow). The indication is that crystals in region (ii) have a unit cell with the lattice parameters larger than those of the initial $SrTiO_3$ layer (i.e. region (i)). The framed region in pattern (iii) suggests the coexistence of $(Sr_{1-x}Ba_x)TiO_3$ (SBT) and $(Ba_{1-x}Sr_x)TiO_3$, where the $(Sr_{1-x}Ba_x)TiO_3$ (BST) reflections are from region (ii)

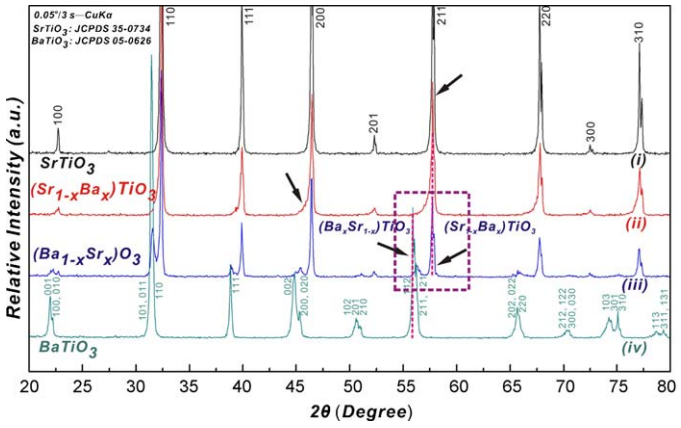

Fig. 2. XRD patterns corresponding to the four regions in Fig. 1, inter-diffused regions are indicated by superimposed and broadened reflections.

because the layer was remained from incomplete grinding due to the concave interface. Peak shift due to the solid solutions formed between $BaTiO_3$ and $SrTiO_3$ is registered in, e.g. {2 1 1}, a line is drawn for reference. The {2 1 1} reflections of $BaTiO_3$ and $SrTiO_3$ have moved towards each other due to solid solutions from inter-diffusion. It is also confirmed from the EDS results from both SEM and TEM, as will be described later.

Fig. 3 shows the XRD pattern of region (iii) from a stack sintered at 1250 °C/20 h (similar to samples shown in Fig. 2, but for a shorter sintering time), which not bonded successfully was separated into two discs. Again, peaks representing $BaTiO_3$ and $SrTiO_3$ have moved towards each other (indicated by arrows), as exemplified by {1 1 0}, {1 1 1}, {2 0 0}, {1 1 2} and {2 2 0}. This suggests an increase of the lattice parameters in $SrTiO_3$ (peaks moving towards lower Bragg angles) and a decrease of such in $BaTiO_3$ (peaks moving towards higher Bragg angles) when they form solid solution due to inter-diffusion.

Additional reflections in region (iii) are indexed to $BaTi_2O_5$ (BT_2), $Ba_4Ti_{13}O_{30}$ (B_4T_{13}), and $Ba_6Ti_{17}O_{40}$ (B_6T_{17}), which are TiO_2-excess compounds often termed polytitanates.

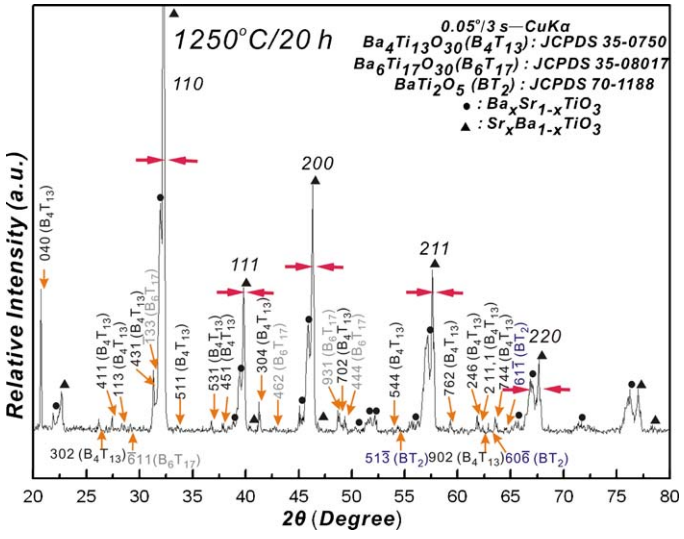

Fig. 3. XRD patterns of the initial $SrTiO_3$–$BaTiO_3$ interface from 1250 °C/20 h samples showing additional polytitanate phases of $BaTi_2O_5$ (BT_2), $Ba_4Ti_{13}O_{30}$ (B_4T_{13}), and $Ba_6Ti_{17}O_{40}$ (B_6T_{17}).

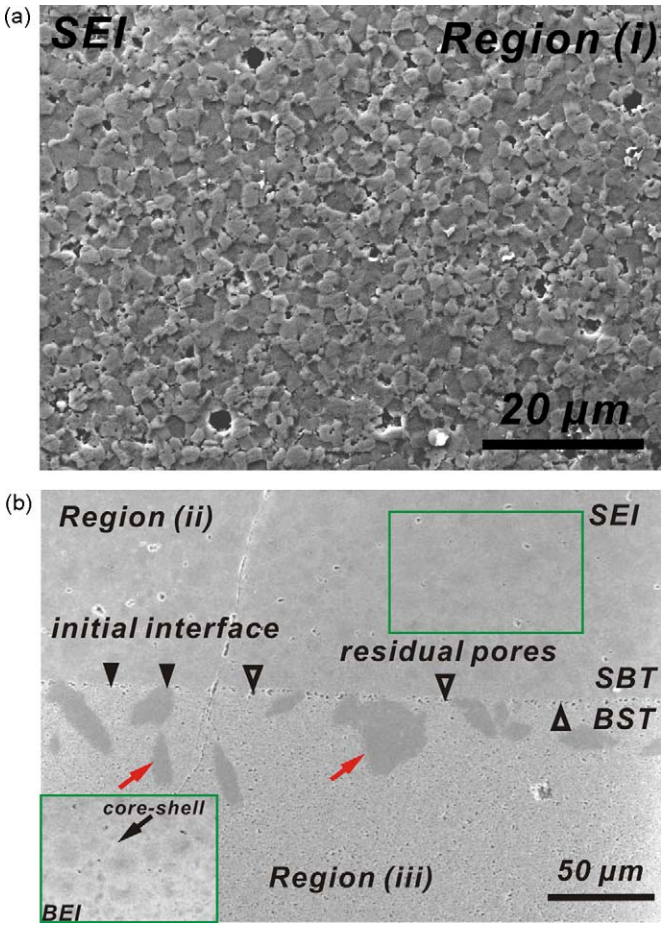

Fig. 4. Microstructure of (a) region (i) represented by uniform $SrTiO_3$ grains, (b) regions (ii) and (iii) separated by residual pores (indicated by unfilled arrowheads) at the initial interface (SEM–SEI) with an inset of the atomic contrast showing solute distribution within core–shell grains containing Sr-rich core and Ba-rich shell (SEM–BEI).

3.2. SEM analysis—microstructure of region (i)

Region (i) of $SrTiO_3$ from a 1250 °C/40 h stack consists of a rather uniform microstructure, as shown by SEM-secondary electron image (SEI) in Fig. 4(a). This region not affected by Ba^{2+} inter-diffusion has retained the initial powder composition of Sr/Ti ≈ 0.99.

3.3. SEM analysis—microstructure of regions (ii) and (iii)

Both regions (ii) and (iii) have been modified by inter-diffusion, which become solid solutions of $(Sr_{1-x}Ba_x)TiO_3$ (SBT) and $(Ba_{1-x}Sr_x)TiO_3$ (BST), respectively. The two regions are separated by an interface containing residual pores of several μm in size, as indicated by unfilled arrowheads in Fig. 4(b). Region (ii) consisting SBT layer of ~300 μm thick is approximately three times greater than region (iii) (BST layer of ~100 μm); the boundaries between layers are also indicated by dotted lines in Fig. 1. The inter-diffusion distance was determined by performing EDS analysis at a 20-μm interval across the $BaTiO_3$–$SrTiO_3$ interface, where the corresponding

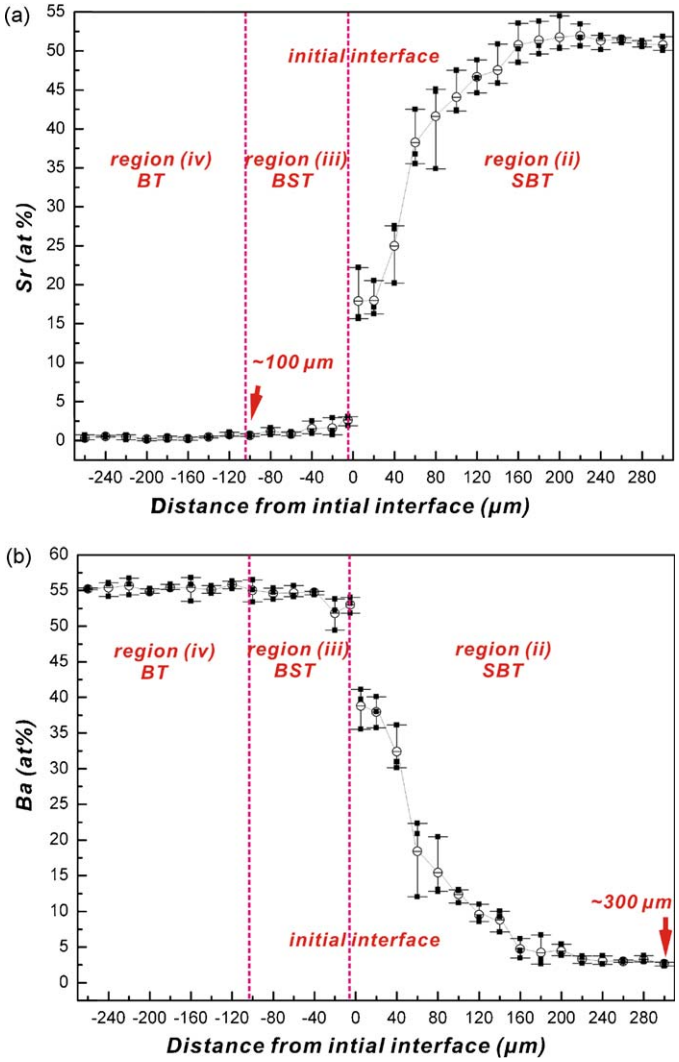

Fig. 5. EDS spectrum showing compositional variation across the initial interface, (a) the Ba-content levels off at ~300 μm, and (b) the Sr-content flattens at ~100 μm.

concentration of Ba and Sr has leveled off, as indicated by arrows in Fig. 5(a) and (b).

Region (ii) contains the characteristic core–shell grains of ~10–20 μm in size with shell enriched in Ba. This is revealed by the atomic contrast from SEM-backscattered electron image (BEI) (shown in the inset in Fig. 4(b)) as well as indicated by EDS microchemical analysis. Inhomogeneous solute distribution is represented by grain A (Fig. 6), containing a core of Sr-rich (34 at% vs 12 at%) and a shell of Ba-rich (34 at% vs 17 at%). Some grains in region (ii), close to the $SrTiO_3$–$BaTiO_3$ interface, exhibit an unusual core–shell structure with faceted boundaries (indicated by filled arrowheads in Fig. 6). These grains covered with irregularly twisted lines and exhibiting a vermicular pattern, are likely to be the 180° ferroelectric domains; they are also richer in Ba (i.e. Sr:Ba = 20 at%:37 at% and 28 at%:33 at% from points indicated by × in Fig. 6(a)), as also revealed by BEI. The A/B-ratios (or ((Ba + Sr)/Ti-ratio) of ~1.32 and ~1.54 also suggest that the vermicular grains contain A-site-excess. Some other grains still contain the 90°

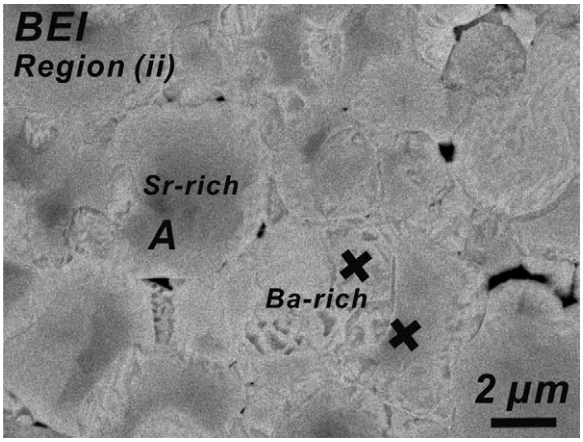

Fig. 6. A characteristic vermicular pattern of $(Sr_{1-x}Ba_x)TiO_3$ grains in region (ii) with grain A containing a Sr-rich core.

$BaTiO_3$ ferroelectric domains characterized by a lamellar feature, as indicated by unfilled arrowheads in Fig. 6.

Region (iii) is separated from region (iv) by the boundary where abnormally grown grains cease to appear (Fig. 1). Its location at ~100 μm is consistent with the EDS spectrum where the Sr-content reaches a plateau, as indicated arrow in Fig. 5(b). Abnormal grains of a polygonal shape and ~200 μm in size are found ubiquitously in region (iv), representing the typical microstructure of undoped $BaTiO_3$ ceramics sintered below the 1332 °C-eutectic temperature [13].

Second phases embedded in a matrix of smaller grains (Fig. 4(b)) are formed along the interface but grown into region (iii) (indicated by unfilled arrowheads in Fig. 1). The second-phase grains contain higher Ti/(Ba + Sr)-ratio of ~2.30 as estimated from an average over eight randomly chosen grains. An average content of Sr at 0.55 at% suggests that they are most likely to be barium polytitanates [16,17], i.e. rich in TiO_2 as compared to $BaTiO_3$, consistent with XRD results (Fig. 3).

Matrix grains in region (iii) also containing a core–shell feature are much smaller at ~0.5 μm in size (Fig. 7(a) and (b)). Such grains were reacting with a large TiO_2-rich grain (indicated). They were being annihilated to become larger second-phase grains (Fig. 7(b)). The concave boundary (indicated by unfilled arrowheads in Fig. 7(a)) suggests that the second-phase grain is growing at the expense of the smaller matrix grains by Ostwald ripening. Matrix grains consisting representatively of core–shell have the ferroelectric domains (indicated by filled arrowheads, where Sr is not detected) and paraelectric shell of higher Sr-content of 4.10 at% are observed.

Microchemical analysis conducted for points 1, 2, and 3 showing variation in the Ti/(Ba + Sr) ratio among a matrix grain (point 1), an annihilated small grain (point 2), and a second-phase grain (point 3), all containing significantly lower Ba-content, is given in the table juxtaposed to Fig. 7(b).

3.4. SEM analysis—microstructure of region (iv)

Abnormally grown grains dispersed in a matrix of refined grains (region (iv) shown in Fig. 1) is the characteristic microstructure of TiO_2-excess $BaTiO_3$ compositions sintered in

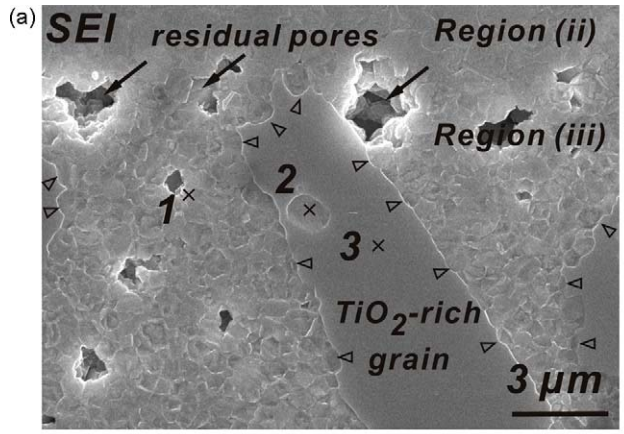

	Ti (at %)	Sr (at %)	Ba (at %)	Ti/(Ba + Sr)
point 1	53.53	4.30	43.17	1.13
point 2	64.30	1.25	34.40	1.80
point 3	68.55	0.55	29.65	2.27

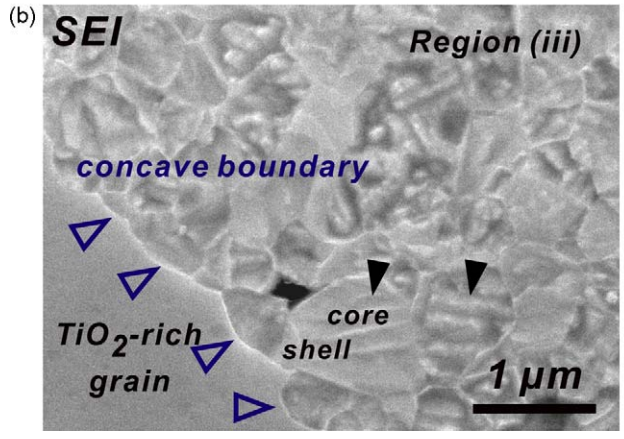

Fig. 7. Core–shell matrix grains (a) reacting with, (b) being annihilated by a growing polytitanate grain in region (iii), and residual pores at regions (ii)–(iii) interface (SEM–SEI), with EDS results shown juxtaposed.

the presence of liquid phase [18]. Such liquid phase is originated from tramp impurities, notably SiO_2, associated with the initial powder and contaminated during sample processing. Some of the abnormal grains (indicated by filled arrowheads in Fig. 1) contain the {1 1 1} double-twin lamellae [15,19]. Although both regions are located in the initially $BaTiO_3$ side, in contrast to region (iii) represented by refined grains and polytitantes, region (iv) containing abnormally grown $BaTiO_3$ grains dispersed in a fine-grain matrix is typical [18] of TiO_2-excess powder sintered at temperatures below the $BaTiO_3$–SiO_2 eutectic at 1260 °C [20].

3.5. TEM analysis of regions (ii) and (iii)

The fact that both regions (ii) and (iii) are represented by grains consisting of a core–shell structure [3,21] is further evidenced by TEM analysis. Type I core–shell consisting a ferroelectric core and a paraelectric shell [3] is more common in region (iii) (BST) while type II containing a superstructure-modulated core [21] encircled by misfit dislocations [3] predominates in region (ii) (SBT). A full analysis will be reported separately [22].

Intragranular voids of <10 nm in size exist superfluously at ~100 μm away from the initial $SrTiO_3$–$BaTiO_3$ interface in grains of region (iii) (containing $Ba_{1-x}Sr_xTiO_3$ (BST) solid solution). The location of the voids was determined by examining a thin foil under OM (Fig. 8(a)), and the area was analyzed further by TEM (Fig. 8(b)), as indicated in both micrographs. Such voids are clustered to approximately three bands (indicated by arrows in Fig. 8(c)), leaving most of the grain regions free of them. This is unambiguously discerned as shown by a strong-beam bright-field (BF) image in Fig. 8(c) where such voids trespassing grain boundaries (as indicated by unfilled arrowheads) is clearly discernible. The framed region is also shown at a higher magnification in Fig. 8(d), most of the intragranular pores (indicated by filled arrowheads) are crystallographically faceted. They are scattered across grain boundaries as can be seen from Fig. 8(c) and (d), a liquid-grain-boundary phase (indicated by unfilled arrowheads) also exists.

4. Discussion

Kirkendall effect [8] induced through inter-diffusion between a diffusion couple manifests itself by the formation of a solid-solution region, by the migration of marker away from the inter-diffusion zone, and by the formation of micro-voids (Kirkendall porosity). An analogy to the original α-brass-Cu diffusion couple is presented here for the $BaTiO_3$–$SrTiO_3$ couple.

A schematic illustration depicting observations of the initial interface, the solid solution region, the marker migration, and the intragranular pores analogous to Kirkendall's effect is shown in Fig. 9.

4.1. Inter-diffusion zone and marker migration

The initial $BaTiO_3$–$SrTiO_3$ interface can be easily discerned by the residual pores caused by differential sintering rates between two layers. The initial interface is where an inert marker could have been placed, as the Mo wires for the α-brass-Cu diffusion couple. Therefore, the residual pores of several micrometres in size (indicated by arrows in Fig. 7(b)) at the initial interface (Figs. 4(b) and 7(b)) are not the Kirkendall porosity, which should have been located in the side containing faster moving cation, i.e. $BaTiO_3$ and Ba^{2+} in region (iii). Because Ba^{2+} diffuses faster than Sr^{2+} [6], marker migration towards the $BaTiO_3$ side is expected [8]. By forming solid solution, the initial interface has indeed moved by ~100 μm towards the $BaTiO_3$ side (region (iii)) until the position where Sr is no longer detected by EDS (Fig. 5(b)). Likewise, the increased volume of solid solution $(Sr_{1-x}Ba_x)TiO_3$ is manifested by forming region (ii) of ~300 μm thick (SBT and shown by arrows in Fig. 1) where the Ba-reading in EDS has leveled off (Fig. 5(a)). The diffusivity of Ba^{2+} is therefore approximately three times faster than that of Sr^{2+} in the respective crystal lattice.

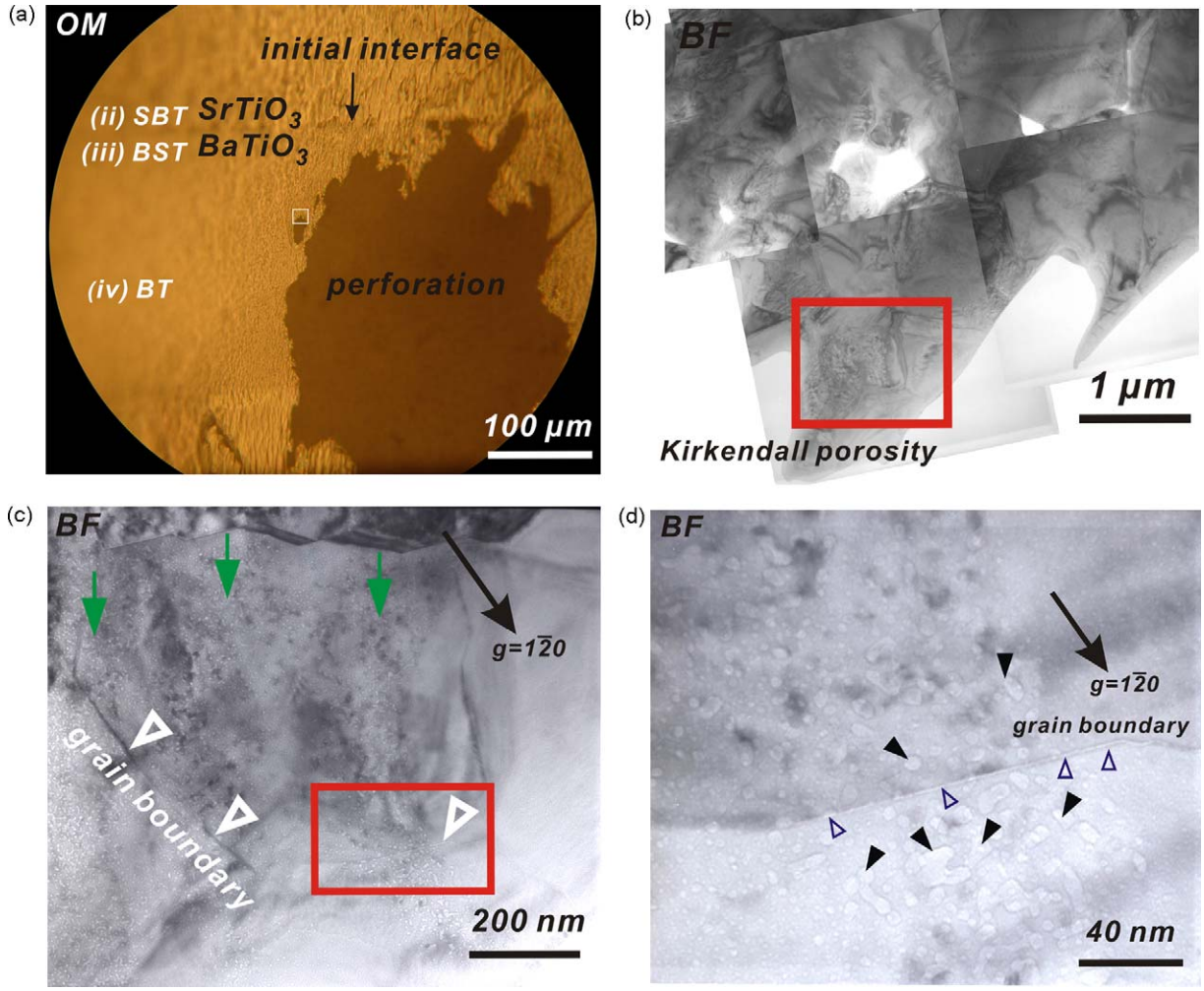

Fig. 8. (a) OM microstructure showing the locations of initial $SrTiO_3$–$BaTiO_3$ interface (shown by an arrow) and Kirkendall pores (framed), (b) the framed region analyzed by TEM, (c) Kirkendall pores clustered in three bands (indicated by arrows) and trespassed grain boundaries, and (d) higher magnification showing faceted pore size at <10 nm (bright-field image-TEM).

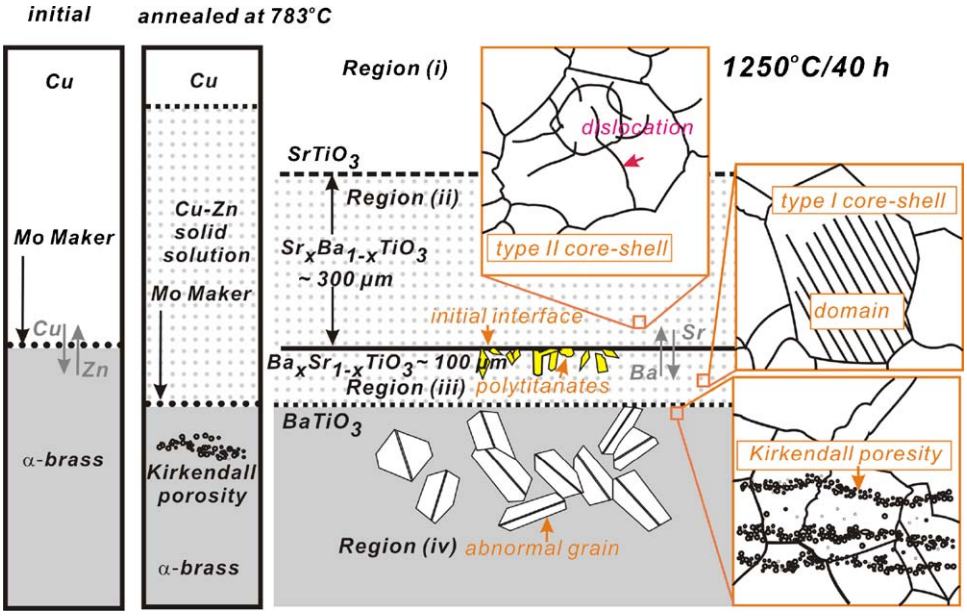

Fig. 9. Schematic diagram illustrates an analogy between the diffusion couples of $SrTiO_3$–$BaTiO_3$ and the original α-brass-Cu, where the location of the Mo makers in the latter is indicated.

Upon annealing at 1250 °C for 40 h, the initial interface has migrated, and then stopped at the Sr^{2+}-diffusion front, i.e. the boundary between region (iii) and (iv) (Fig. 1). Analogously, the solid-solution region of (BST + SBT), equivalent to Cu–Zn alloy in Kirkendall's original diffusion couple (Fig. 9), has increased its volume from initially non-existent to that consisting of regions (ii) and (iii) of all together ~400 μm thick (i.e. ~100 + 300 μm). Forming solid solution in the $BaTiO_3$–$SrTiO_3$ diffusion couple has also produced distinctive core–shell microstructures on either side of the initial interface due to inward diffusion of Ba^{2+} and Sr^{2+} into the respective grains.

Further, Sr^{2+} doping through inter-diffusion has effectively suppressed the abnormal grain growth [18] in the initial $BaTiO_3$ layer, as demonstrated in region (iii). Since the core–shell structure is also associated with the characteristic diffuse-phase-transition dielectric behavior of CaO-doped $BaTiO_3$ multi-layer ceramic capacitors [21], combining with grain refinement, they may provide insights into how tunable microwave properties [1,2] are developed.

4.2. Kirkendall porosity

The inter-diffusion coefficient can be derived by treating the quaternary diffusion couple of ABO_3-$A'BO_3$ as a pseudo-binary, where perovskite is described by the general formula of ABO_3, both A and A′ are A-site cations. Gopalan et al. [6], suggested that two limiting cases are possible from differential diffusivities: (a) D_A, $D_{A'} \gg D_O$, D_B, where A-site cations are the faster diffusing species, and (b) D_A, $D_{A'} \ll D_O$, D_B, where A-site cations diffuse slower.

For case (a), the lattice velocity becomes negligible and the diffusion follows Nernst–Planck behaviour. When inter-diffusion only occurs on the A-site sublattice, e.g. Ca^{2+} and Sr^{2+}, there is no Kirkendall effect. This was concluded [5] for sintered $CaTiO_3$–$SrTiO_3$ couple since no Kirkendall pores were detected.

The Kirkendall effect [8] occurs in case (b) because the limiting inter-diffusion coefficient follows Darken behaviour [6]. Such behaviour is only possible when the diffusivities of oxygen and B-site cation (i.e. D_O and D_B) are not much greater than those of the A-site cations (i.e. D_A and $D_{A'}$). All species are mobile that the lattice velocity is non-zero and the diffusion is molecular. Examining the annealed microstructure of La^{3+}-donor-doped $SrTiO_3$–$BaTiO_3$ couple [6] suggests that Kirkendall porosity is located in the $BaTiO_3$ side. By an analogy to the original α-brass-Cu diffusion couple [8], it implies that Ba^{2+} diffuses via a vacancy mechanism at a faster rate than Sr^{2+} in both $SrTiO_3$ and $BaTiO_3$ lattice [5,6]. This is consistent with the present results where the thicknesses of regions (ii) and (iii) by the ratio of ~3:1 (i.e. diffusivity of Ba^{2+} and Sr^{2+} at 3:1) are determined from microchemical analysis (Fig. 5(a) and (b)).

Voids are three-dimensional aggregates of vacancies. The formation of Kirkendall porosity is easily perceived in metals and alloys [8,23] since only metal atoms are involved in diffusion. However, it requires both cation vacancies and oxygen vacancy of concentrations in 1:1:3 of the stoichiometric composition to form a molar void of $BaTiO_3$ intragranularly, i.e. a unit cell of negative $BaTiO_3$ crystal, with Ba^{2+} being faster diffusing [10,11]. Therefore, like in sintering the vacancies must arrive at the same site simultaneously when the slowest moving ion diffusing at its fastest path is rate-controlling kinetically. Oxygen diffuses rapidly along grain boundaries, and V''_{Ba} is made available from Ba^{2+} migrating to the $SrTiO_3$ side by inter-diffusion. Even when Ti^{4+} diffusion via V''''_{Ti} is the slowest moving path in perovskite [11], the observation of such voids confirms that molecular diffusion has occurred [6] in $BaTiO_3$–$SrTiO_3$ couple. That is to say, all species between region (i) and (iv) have moved towards each other [6], instead of just the A-site cation [5]. Indeed, the voids (Fig. 8(b)–(d)) are found in the vicinity of Kirkendall plane at ~100 μm where Sr is no longer detected (Fig. 5(b)). Regardless of the individual diffusivity, the lattice as a whole has moved from the $BaTiO_3$ side to $SrTiO_3$, following Darken behaviour, and leaving behind Kirkendall voids within $BaTiO_3$ grains. The Sr^{2+} diffusion front separating region (iii) from (iv) therefore represents the Kirkendall plane. If an inert marker had been placed at the initial $BaTiO_3$–$SrTiO_3$ interface, which is where it should have migrated.

The cavities of several micrometers in size (Fig. 7(b)) located along the initial $BaTiO_3$–$SrTiO_3$ interface (Fig. 1), nevertheless, are residual pores from sintering, not Kirkendall porosity. They are the result of differential sintering when the $BaTiO_3$ side of the initial interface is under tension, as suggested by the inward curvature of the $BaTiO_3$ layer indicated in Fig. 1.

As a result, an extensive region of BST and SBT solid solution is produced, consistent with the Kirkendall effect. Nevertheless, unlike those in α-brass-Cu couple where only Zn vacancies are involved in the formation, Kirkendall porosity in $BaTiO_3$ layer (region (iii)) is generated from the condensation of both cation vacancies and oxygen vacancy at the ratio of 1:1:3.

4.3. Second-phase grains at initial interface

TiO_2-rich second-phases [7] (Fig. 7(a) and (b)) were produced from reaction between $BaTiO_3$ with TiO_2 in the vicinity of the initial $BaTiO_3$–$SrTiO_3$ interface. Concave boundaries (indicated by unfilled arrowheads (Fig. 7(b)) with the side number $n > 6$ suggesting growing grains can be seen from the polytitanate grains. The excessive TiO_2 may have been provided by inter-diffusion from both sides of the stack. Subsequent reaction with the matrix grains of BST can be seen from Fig. 7(b) where a small, intragranularly located grain (grain 2) is being annihilated by the large grain containing significantly higher TiO_2 (grain 3).

5. Conclusions

An inter-diffusion study by sintering ceramic stacks at 1250 °C in air indicates that Kirkendall effect has occurred between the $BaTiO_3$–$SrTiO_3$ diffusion couple. TiO_2-rich polytitanates detected at the initial interface also derive from

inter-diffusion. We propose an analogy between the diffusion couples of $BaTiO_3$–$SrTiO_3$ and the original α-brass-Cu. This is based on crystalline phase identification, microchemical analysis and microstructure observation, viz. (1) four distinctive regions of crystalline phases, corresponding microstructures, chemical compositions are developed after sintering, (2) volume increase of the initial $SrTiO_3$ side by forming solid solution $(Ba_{1-x}Sr_x)TiO_3$ with $BaTiO_3$, (3) the thicknesses of the inter-diffused layers $(Sr_{1-x}Ba_x)TiO_3$ and $(Ba_{1-x}Sr_x)TiO_3$ by a ∼3:1 ratio indicating Ba^{2+} is the faster diffusing A-site cation, and most important, (4) the Kirkendall porosity detected at ∼100 μm in the $(Ba_{1-x}Sr_x)TiO_3$ region due to molecular diffusion and the condensation of both cation vacancies and oxygen vacancy in $BaTiO_3$.

Acknowledgement

We thank the National Science Council of Taiwan for funding support through contract NSC-9502221-E-033-MY3.

References

[1] A.K. Tagantsev, V.O. Sherman, K.F. Astafiev, J. Venkatesh, N. Setter, Ferroelectric materials for microwave Tunable applications, J. Electroceram. 11 (1) (2003) 5–66.
[2] S.A. Wolf, D. Treger, Frequency Agile Materials for electronics—progress in the DARPA programme, Integrat. Ferroelectrics 42 (1) (2002) 39–55.
[3] H.Y. Lu, J.S. Bow, W.H. Deng, Core–shell structures in ZrO_2-modified $BaTiO_3$ ceramics, J. Am. Ceram. Soc. 73 (12) (1990) 3562–3568.
[4] J.S. Kim, S.J.L. Kang, Formation of core–shell structure in the $BaTiO_3$–$SrTiO_3$ system, J. Am. Ceram. Soc. 82 (4) (1999) 1085–1088.
[5] E.P. Butler, H. Jain, D.M. Smyth, Cation interdiffusion in calcium and strontium titanate, J. Am. Ceram. Soc. 74 (4) (1991) 772–776.
[6] S. Gopalan, A.V. Virkar, Interdiffusion and Kirkendall effect in doped $BaTiO_3$–$SrTiO_3$ diffusion couples, J. Am. Ceram. Soc. 78 (4) (1995) 993–998.
[7] D. Kolar, M. Trontelj, Z. Stadler, Influence of interdiffusion on solid solution formation and sintering in the system $BaTiO_3$–$SrTiO_3$, J. Am. Ceram. Soc. 65 (10) (1982) 470–474.
[8] E.O. Kirkendall, Diffusion of zinc in alpha brass, Trans. Am. Inst. Min. Metall. Eng. 147 (2) (1942) 104–110.
[9] M.J.H. van Dal, M.C.L.P. Pleumeekers, A.A. Kodentsov, F.J.J. van Loo, Intrinsic diffusion and Kirkendall effect in Ni–Pd and Fe–Pd solid solutions, Acta Mater. 48 (2) (2000) 385–396.
[10] A. Yamada, Y.M. Chiang, Nature of cation vacancies formed to compensate donors during oxidation of $BaTiO_3$, J. Am. Ceram. Soc. 78 (4) (1995) 909–914.
[11] Y.M. Chiang, T. Takagi, Grain-boundary chemistry of $BaTiO_3$ and $SrTiO_3$. II. Origin of electrical barrier in positive-temperature coefficient thermistors, J. Am. Ceram. Soc. 73 (11) (1990) 3286–3291.
[12] G.V. Lewis, C.R.A. Catlow, Computer modelling of $BaTiO_3$, Radiat. Eff. 73 (1/4) (1983) 307–314.
[13] K.W. Kirby, B.A. Weschler, Phase relations in the $BaTiO_3$–TiO_2 system, J. Am. Ceram. Soc. 74 (8) (1991) 1841–1847.
[14] R. Raj, R.K. Bordia, Sintering behaviour of Bi-modal powder compacts, Acta. Metall. 32 (7) (1984) 1003–1019.
[15] Y.C. Wu, C.C. Lee, D.E. MaCauley, M.S.H. Chu, H.Y. Lu, The {1 1 1} growth twins in tetragonal barium titanate, J. Am. Ceram. Soc. 89 (5) (2006) 1679–1686.
[16] E. Tillmanns, W. Hofmeister, W.H. Bauer, Variations on the theme of closest packing: the structural chemistry of barium titanate compounds, J. Solid State Chem. 58 (1) (1985) 14–28.
[17] J.J. Ritter, R.S. Roth, J.E. Blendell, Alkoxide precursor synthesis and characterization of phases in the Ba–Ti oxide system, J. Am. Ceram. Soc. 69 (2) (1986) 155–162.
[18] D.F.K. Hennings, R. Janssen, P.J.L. Reynen, Control of Liquid-phase-enhanced discontinuous grain growth in barium titanate, J. Am. Ceram. Soc. 70 (1) (1987) 23–27.
[19] H. Oppolzer, H. Schmelz, Investigation of twin lamella in $BaTiO_3$, J. Am. Ceram. Soc. 66 (6) (1983) 444–446.
[20] D.E. Rase, R. Roy, Phase equilibrium in the system $BaTiO_3$–SiO_2, J. Am. Ceram. Soc. 38 (11) (1955) 389–395.
[21] Y.C. Wu, D.E. McCauley, M.S.H. Chu, H.Y. Lu, The {1 1 1} modulated domains in t-$BaTiO_3$, J. Am. Ceram. Soc. 89 (9) (2006) 2702–2709.
[22] H.W. Lee, C.Y. Siao, H.Y. Lu, Core–shell structure and superlattice phase in the inter-diffusion layers of $BaTiO_3$–$SrTiO_3$ diffusion couple, 2008, unpublished results.
[23] A.J.E. Foreman, H.S. von Harrach, D.K. Saldin, The TEM contrast of faceted pores, Philos. Mag. (A) 45 (4) (1982) 625–645.